Supplementary Information

Methods

Preparation of sintered pellets. To fabricate polycrystalline dense samples, hydrothermally prepared nanocrystalline $BaTiO_3$ powders (Samsung Fine Chemicals Co.) with 60, 110, and 220 nm size were used. Seven oxide-type additives, MnO (99%, Alfa Aesar), Fe_2O_3 (>98%, Sigma Aldrich), NiO (99.8%, Sigma Aldrich), CoO (99.99%, Sigma Aldrich), Al_2O_3 (99.99%, Sigma Aldrich), Ga_2O_3 (>99.99%, Sigma Aldrich), and In_2O_3 (>99.9%, Sigma Aldrich) were utilized for a conventional mixed-oxide technique. The molar ratio between $BaTiO_3$ and each additive oxide was 98:2 for MnO, 99:1 for Fe_2O_3 and In_2O_3, 95:5 for NiO and CoO, and 97.5:2.5 for Al_2O_3 and Ga_2O_3 to achieve sufficient grain growth inhibition. Each powder mixture of $BaTiO_3$ and an additive together with 0.5 wt% SiO_2 (99.5%, Sigma Aldrich) was ball-milled with zirconia balls in high-purity ethyl alcohol for 24 h. Dried powder mixtures were slightly pressed into disks and then isostatically pressed under 200 MPa. The disk pellets were sintered at 1200°C for 1 h in $0.5H_2-99.5N_2$ (500 sccm). In-added samples were sintered at a slightly elevated temperature, 1220°C, for better densification. A fast-firing process with a heating rate of 80°C/min was adopted to suppress the grain growth. An identical rate was applied for cooling as well. The relative density of sintered samples was measured to be 93–96% by the Archimedes method. X-ray diffractometry (D/MAX-2500, Rigaku) with Cu K_α radiation was also carried out to investigate both the peak position variation and the tetragonality of sintered samples.

STEM, EDS, and SEM. Samples for STEM observation were prepared from densely sintered polycrystals by lift out via ion-beam milling in a focused ion beam system (Quanta 3D FEG and Helios G4 UX, Thermo Fisher Scientific). Z-contrast HAADF-STEM images were taken with transmission electron microscopes (Titan cubed G2 60-300 and Spectra Ultra 30-300, Thermo Fisher Scientific) at 300 kV with a spherical aberration corrector (CEOS GmbH). The optimum size of the electron probe was ~1 Å with a convergence semiangle of 19 mrad. The collection semiangles of the HAADF detector were set to be 67.6–200 mrad in order to exploit large-angle elastic scattering of electrons for clear Z-sensitive images. ABF images were also obtained in Spectra Ultra 30-300 at 200 kV. The obtained raw images were band-pass filtered to reduce background noise. For an atomic-column-resolved EDS analysis, both Spectra Ultra 30-300 with four integrated silicon-drift detectors (SDDs) for a 4.04 srad solid angle at a beam current of 100–150 pA and JEM-ARM300F2 (JEOL) with large-sized dual SDDs (158 mm^2) at a beam current of 30–200 pA were used at 200 kV. Chemical-composition mapping by EDS at low magnifications was performed in a Talos F200X (Thermo Fisher Scientific) at a high beam-current rate of 1.6 nA/cm^2 at 200 kV for efficient and rapid acquisition of X-ray signals. The overall polycrystalline microstructure of the samples was observed in a scanning electron microscope (SU5000, Hitachi). The size of more than 100 grains was measured in each of the samples to determine the average grain size.

Electrical properties. Samples with dimensions of $0.5 \times 0.5 \times 3$ mm^3 were used along with Ag paste as electrodes to measure the dielectric properties including relative permittivity and dialectic loss as a function of frequencies and temperature. For these measurements, impedance analyzers (E4990A and E4991B, Keysight) with a voltage of 0.5 V$_{rms}$ were utilized to cover a wide range of frequencies up to 1 GHz. In addition to the nominal relative permittivity, the *effective* permittivity values under a DC electric field up to 8 V/μm were recorded by using a power device analyzer (TF 2000, axiACCT Systems GmbH) at 1 kHz with 5 V ac amplitude. The temperature-dependent permittivity and dissipation loss in each sample were also measured at 1 kHz. The ferroelectric polarization variation as a function of the electric fields was also recorded by the TF 2000 in a ferroelectric hysteresis testing mode in a range of ±65 kV/cm with a frequency of 100 Hz. The insulation resistance was also measured with a high resistance meter (4339B, Hewlett-Packard) at room temperature by applying DC voltage. To maximize the capacitance and simultaneously prevent leakage current in a ceramic capacitor, the insulation resistance (IR), which is parallel to the capacitance component in the equivalent circuit, should be sufficiently large. The IR values of our acceptor-added samples are in an order of 10^{11-12} Ω·cm, verifying high insulation behavior.

DFT calculations. *Ab initio* DFT calculations were carried out within the generalized-gradient approximation (GGA) along with the PBEsol functional revised for exchange correlation of densely packed solids and the ultrasoft pseudopotentials for ionic cores, as implemented in the CASTEP code (Biovia). We constructed a GB supercell, in which two BaTiO$_3$ crystals with different projections ([100] and [110]) are in contact with each other across the GB. The plane-wave basis set for a kinetic energy cutoff was 450 eV. Relaxation of the internal coordinates for each atom in the relaxation layer was performed using the BFGS algorithm with convergence tolerances of 0.1 eV/Å for the maximum ionic force, 5×10^{-5} eV/atom for the total energy, and 0.005 Å for the maximum ionic displacement.

Supplementary Note S1

Hillert[S1] in 2004 derived a new solute drag equation applicable to multicomponent systems. It begins from the force balancing on the migrating interface, as suggested by Cahn[S2] in 1962:

$$P^{\text{sd}} + P^{\text{friction}} + P^{\sigma} = 0 \tag{1}$$

where P^{sd} represents the net attractive force of solute atoms with the interface, P^{friction} is the intrinsic resistance to the interface migration, and P^{σ} is the interfacial tension caused by the curved interface, being positive in the case of growing grains. If Eq. (1) is multiplied by the molar volume, on the basis of energy Eq. (2) is obtained as follows.

$$P^{\text{sd}} V_{\text{m}} + P^{\text{friction}} V_{\text{m}} + P^{\sigma} V_{\text{m}} = 0 \tag{2}$$

Lücke and Stüwe[S3] in 1971 represented the first term of Eq. (2) by introducing the potential variation of solute B within the interface and gave the following equation:

$$P^{\text{sd}} V_{\text{m}} = - \int_{-\infty}^{\infty} x_B \frac{\mathrm{d}E}{\mathrm{d}\xi} \mathrm{d}\xi \tag{3}$$

where E is the potential of the solute B and ξ is the length coordinate. Because E varies only within the interface, a range of integration over the width of the interface from $\xi = 0$ to $\xi = \delta$ is sufficient. Cahn[S2] also gave the following equivalent equation, as x_B is constant.

$$P^{\text{sd}} V_{\text{m}} = - \int_{-\infty}^{\infty} (x_B - x_B^o) \frac{\mathrm{d}E}{\mathrm{d}\xi} \mathrm{d}\xi \tag{4}$$

By considering $E = \Delta\mu_B - \Delta\mu_A$ in a binary system, Eq. (4) can be written as the following equation.

$$
\begin{aligned}
P^{\text{sd}} V_{\text{m}} &= - \int_{-\infty}^{\infty} (x_B - x_B^o) \frac{\mathrm{d}(\Delta\mu_B - \Delta\mu_A)}{\mathrm{d}\xi} \mathrm{d}\xi \\
&= - \int_{0}^{\delta} (x_B - x_B^o) \frac{\mathrm{d}\Delta\mu_B}{\mathrm{d}\xi} \mathrm{d}\xi - \int_{0}^{\delta} (x_A - x_A^o) \frac{\mathrm{d}\Delta\mu_A}{\mathrm{d}\xi} \mathrm{d}\xi.
\end{aligned}
\tag{5}
$$

This relation shows that both the solute (B) and solvent (A) are treated in the same way. As a result, a general equation for the solute drag in a multicomponent system can be derived from Eq. (5) as follows:

$$P^{\text{sd}} V_{\text{m}} = - \int_{0}^{\delta} \sum x_i \frac{\mathrm{d}\Delta\mu_i}{\mathrm{d}\xi} \mathrm{d}\xi \tag{6}$$

where P^{sd} represents the net dragging force caused by the ith component against the interface migration, V_m is the molar volume, x_i, is the composition of the ith component in a multicomponent system, μ_i is the chemical potential of the ith component, ξ is the length coordinate, and δ is the width of the interface. It is thus necessary to integrate over the width of the interface from $\xi = 0$ to $\xi = \delta$ to consider the total dragging force by each component. It is apparent from this Hillert equation (Eq. 6) that any large chemical potential variation, $d\Delta\mu_i/d\xi$, at grain boundaries from $\xi = 0$ to $\xi = \delta$ will exert a strong dragging force at the interfaces in a multicomponent system. Therefore, the grain-boundary segregation of Ba vacancies, not only indium solutes, should play a significant role in impeding the grain-boundary migration in In-added $BaTiO_3$.

Supplementary references

S1. M. Hillert, *Acta Mater.*, 2004, **52**, 5289–5293
S2. J. W. Cahn, *Acta Metall.*, 1962, **10**, 789–798.
S3. K. Lücke and H. P. Stüwe, *Acta Metall.*, 1971, **19**, 1087–1099.
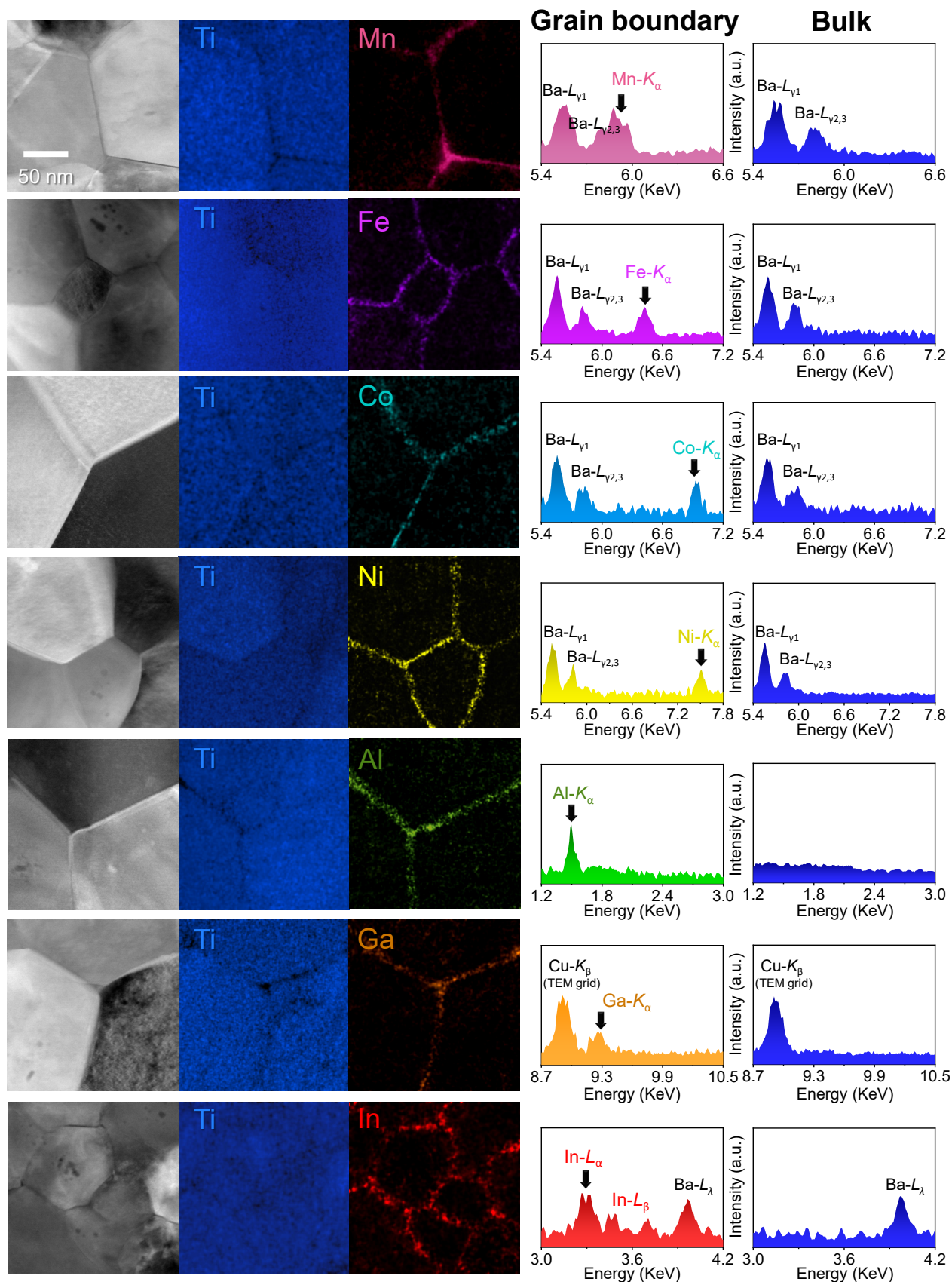
Figure S1. Additional sets of EDS maps and extracted EDS spectra of the GB region in each polycrystalline sample. Further HAADF images and EDS maps are provided to verify the GB segregation of each additive. As consistently supported by the EDS spectra, the additives are distributed exclusively at GBs rather than inside the bulk grains.
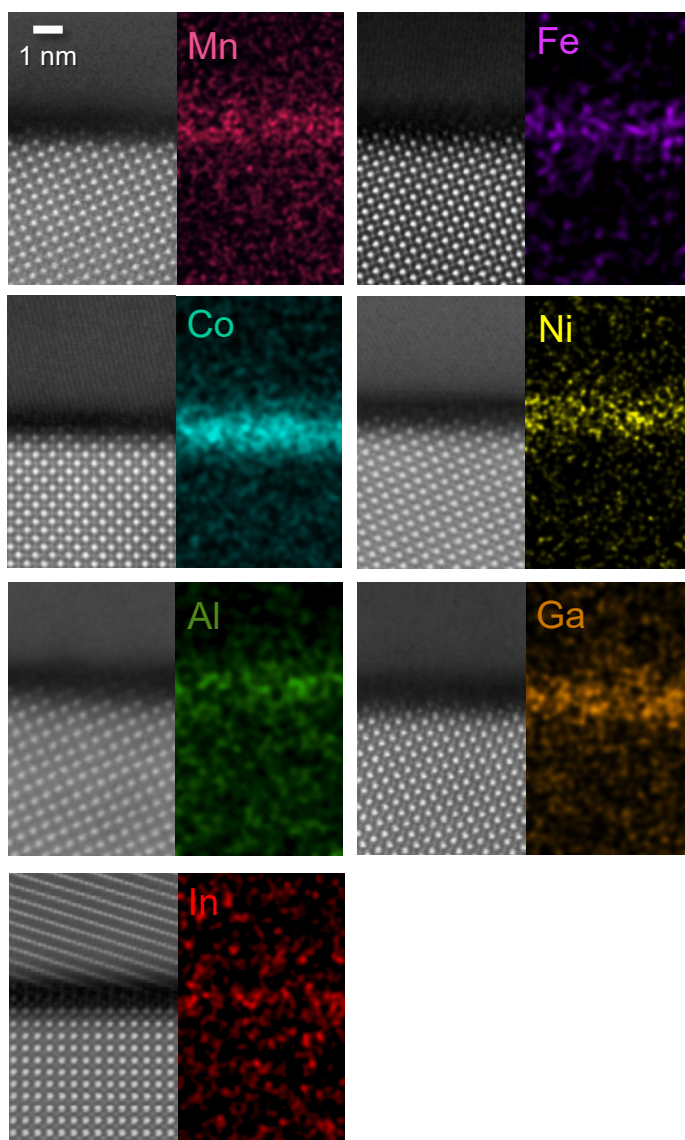
Figure S2. Additional sets of nanoscale EDS maps. Further atomic-level HAADF images and EDS maps are provided to demonstrate the nanoscale width of GB segregation for all the additives. These STEM images also clarify that GBs are free from any dopant-rich secondary phases.
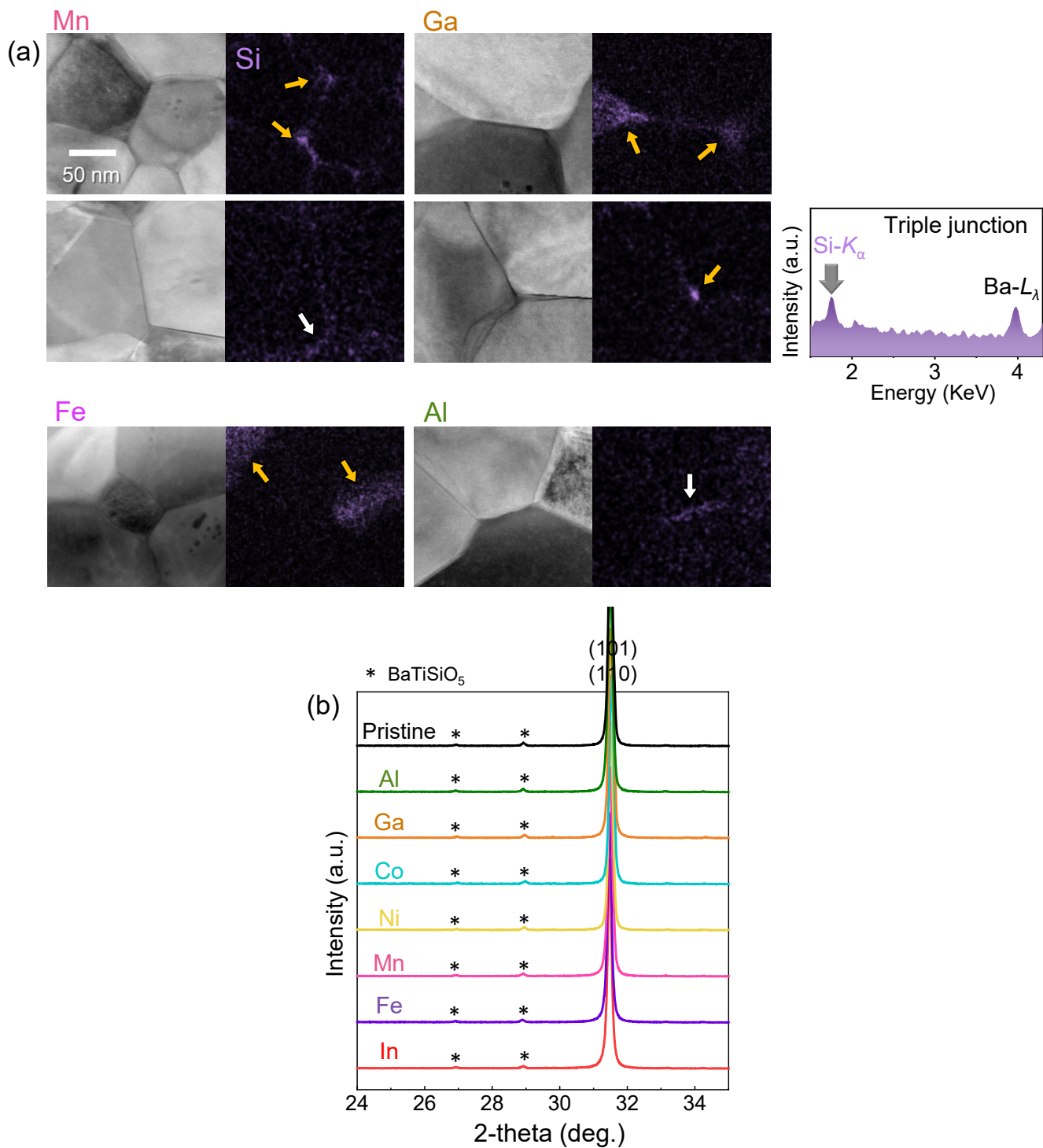
Figure S3. Additional sets of nanoscale EDS maps and X-ray diffraction patterns. (**a**) The presence of Si was identified in all of the samples during EDS mapping. The Si-rich phase was largely observed at three-grain junctions and grain boundaries as a discrete secondary phase. (**b**) The presence of $BaTiSiO_5$ phase was verified by X-ray diffractometry, as denoted by asterisks.

In
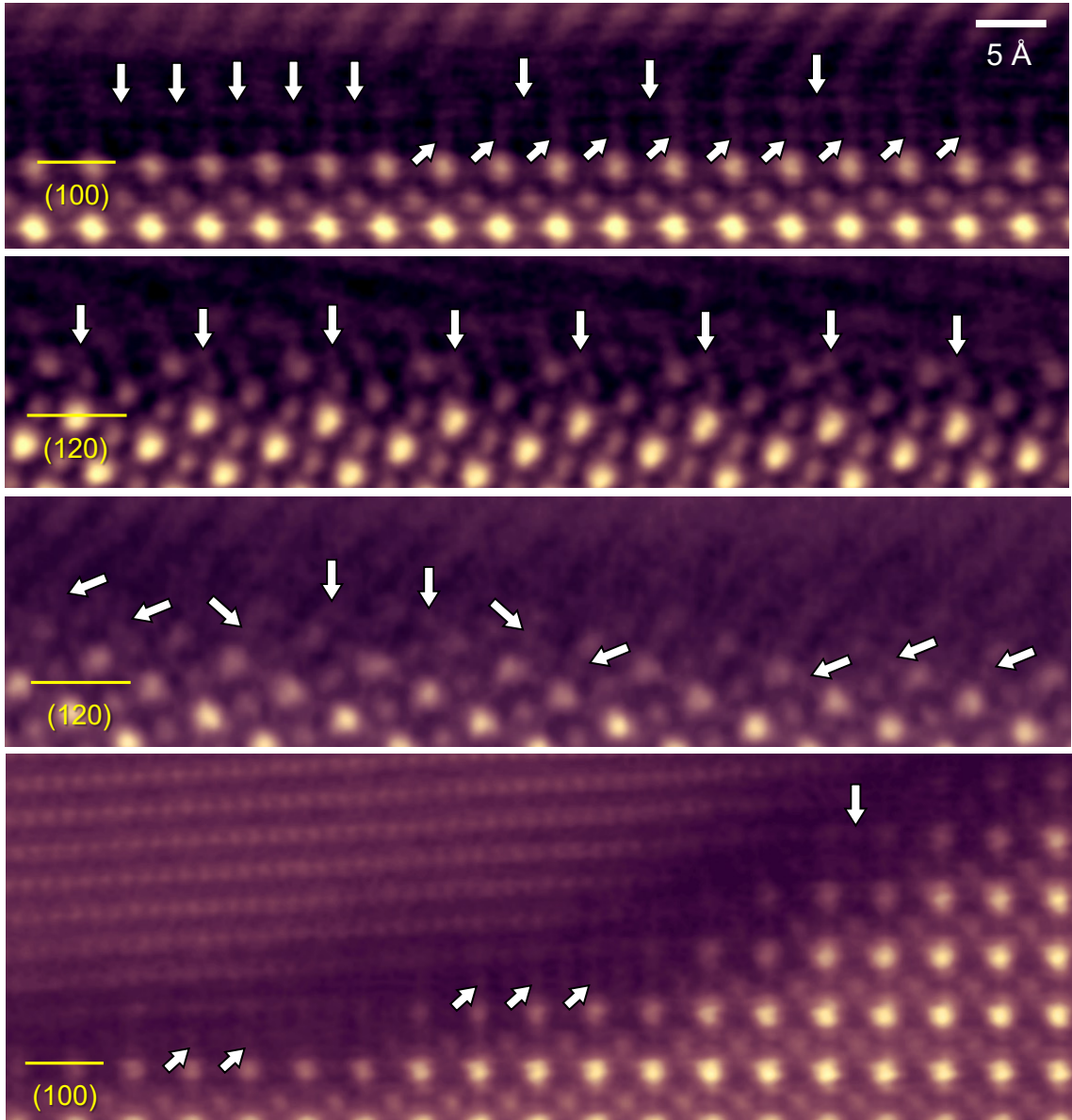
Figure S4. Atomic-column-resolved HAADF-STEM images for GB regions in the In-added sample. White arrows in each image indicate the columns with a detectable intensity for the square-planar interstices. In particular, as denoted by arrows in the first and second images, a periodic array of the interstice columns is noted, indicating that this ordering configuration of In is more stable than random arrangement at GBs.
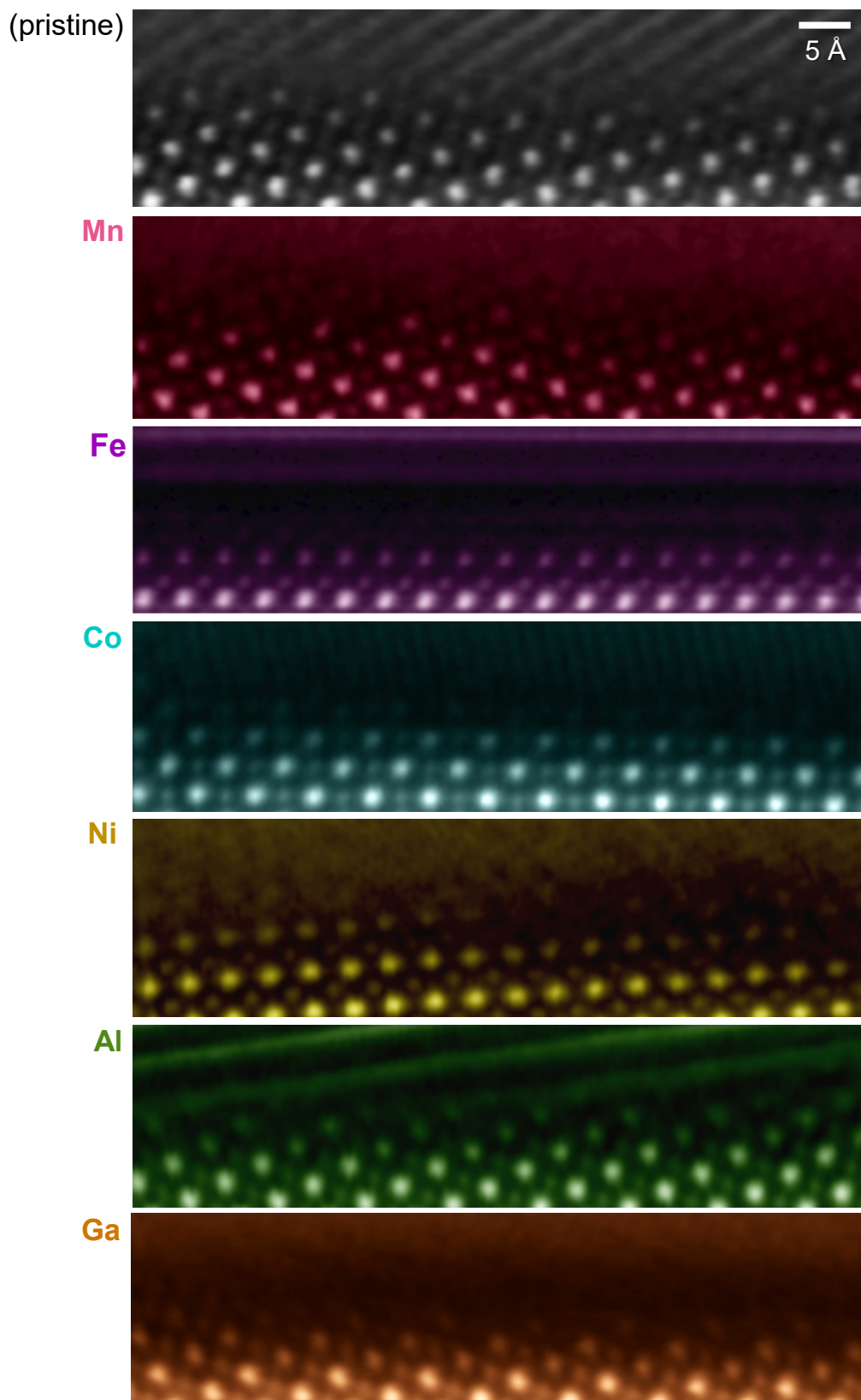
Figure S5. Representative atomic-scale HAADF-STEM images for GB regions in the samples with Mn, Fe, Co, Ni, Al, and Ga. The image for a pristine sample is also shown as a reference. As demonstrated in this series of images, typical atomic structure of the perovskite framework was identified without any detectable contrast in the unusual interstitial sites in the samples with the six additives.
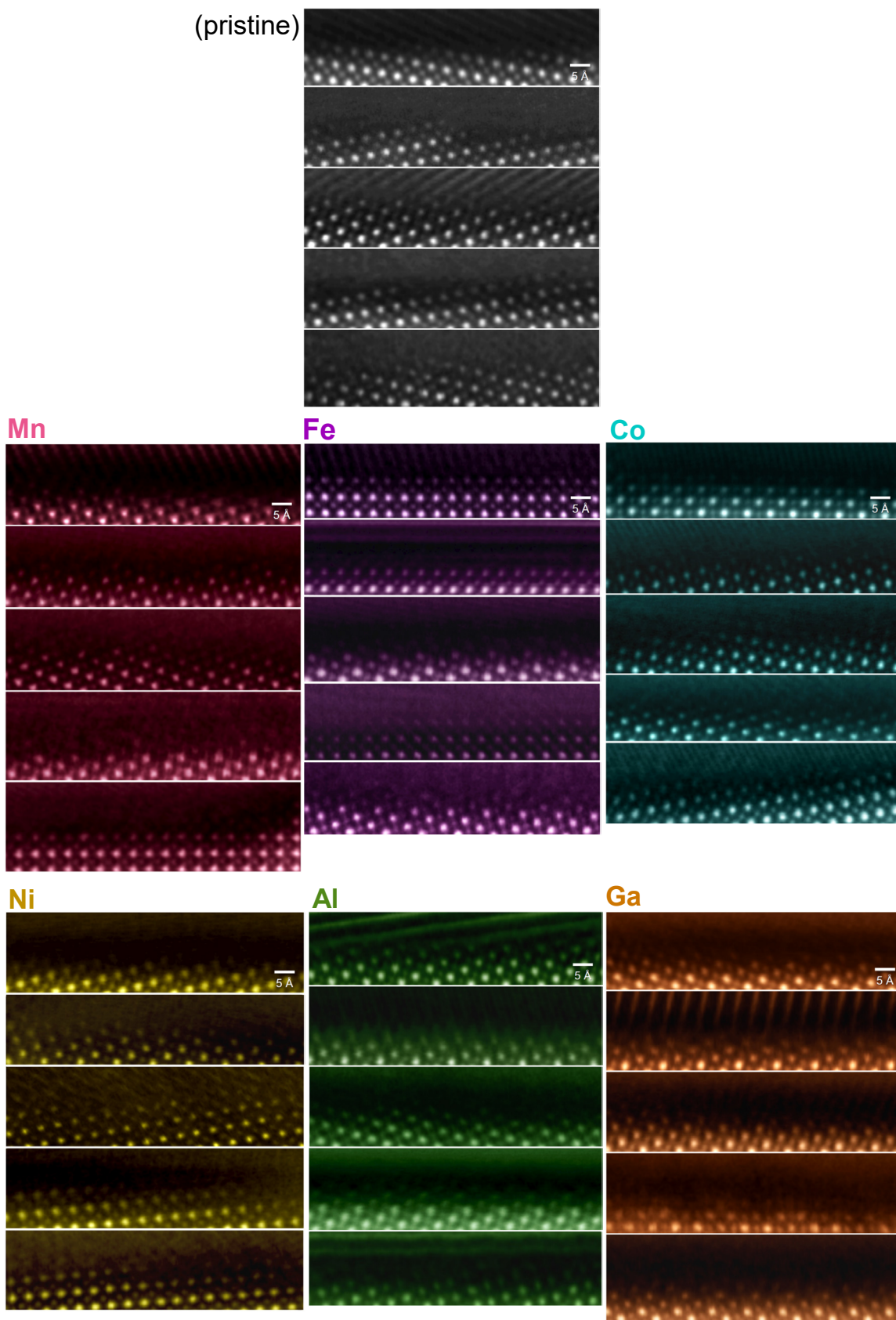
Figure S6. Additional sets of atomic-level HAADF-STEM images for GB regions in the samples with the six additives. In contrast to the STEM observations in the In-added case, no column occupation at the square-planar interstices is identified in the samples with the six additives.

Ba-deficient GBs
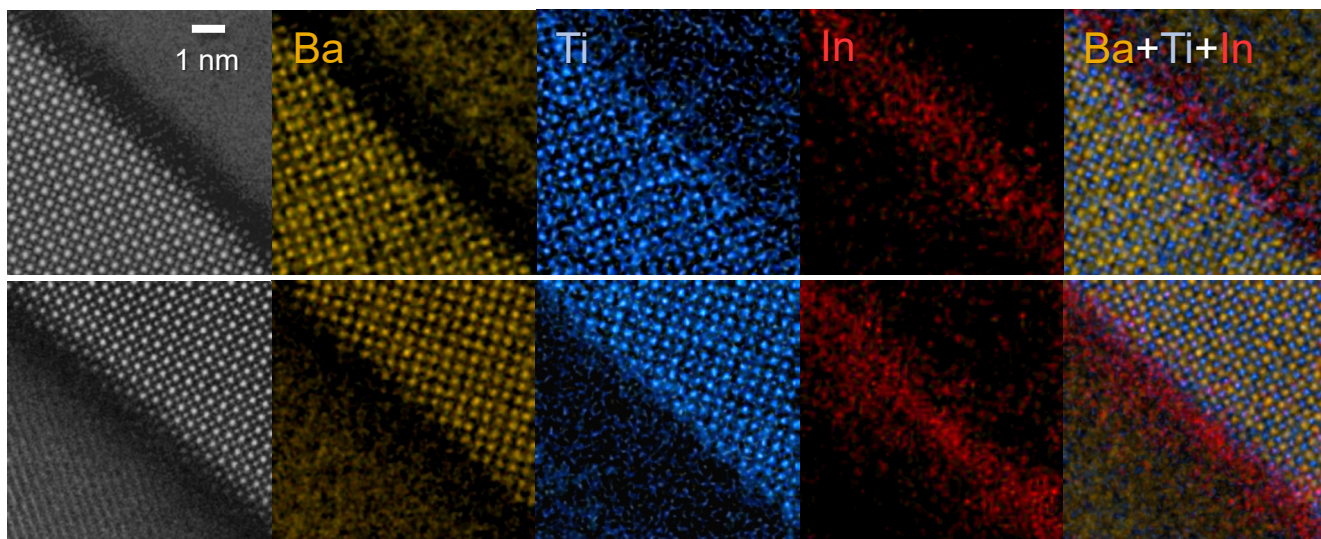
Figure S7. Additional atomic-scale EDS maps for GB region in the In-added samples. These independent GBs consistently demonstrate a considerably Ba-deficient composition in addition to strong In segregation at the GBs. This set of EDS maps thus provides important evidence to consolidate that the Ba-deficient composition is not merely limited to certain special GBs but rather a general feature.
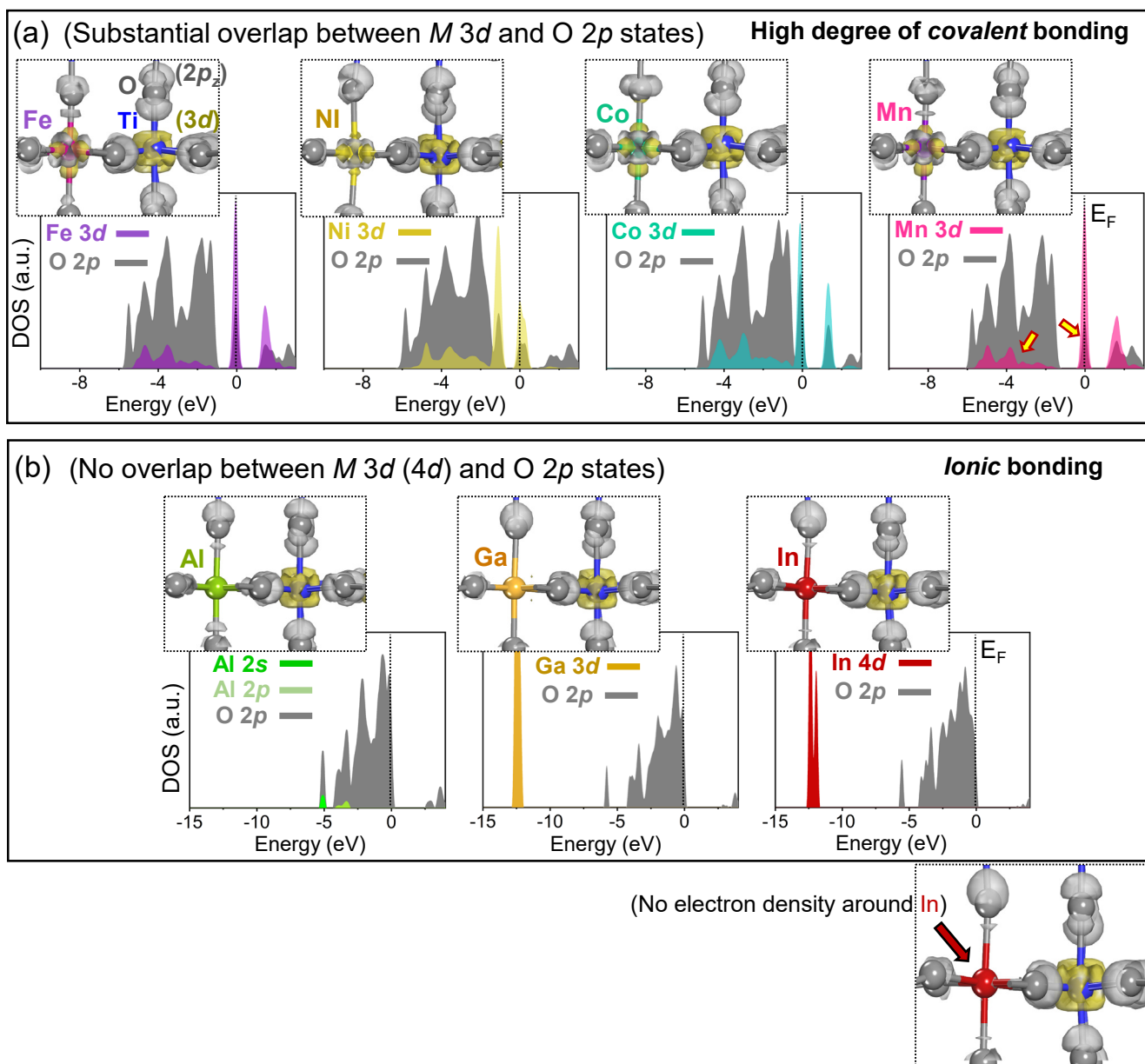
Figure S8. Entire set of electron-density isosurface contours and DOS plots for the seven dopants. (**a**) For the four transition-metal dopants, Fe, Ni, Co, and Mn, a substantial overlap between the O 2p and transition-metal 3d states beneath the Fermi level in the DOS plots is noted to be a common aspect, indicating a comparatively high degree of covalent bonding characteristics. (**b**) For the other three dopants, Al, Ga, and In, there is no overlap between the O 2p and metal d states in the DOS plots. Therefore, while significant electron density around oxygen is presented, no substantial isosurface contours are represented around Al, Ga, and In atoms, showing ionic bonding nature in Al–O, Ga–O, and In–O.
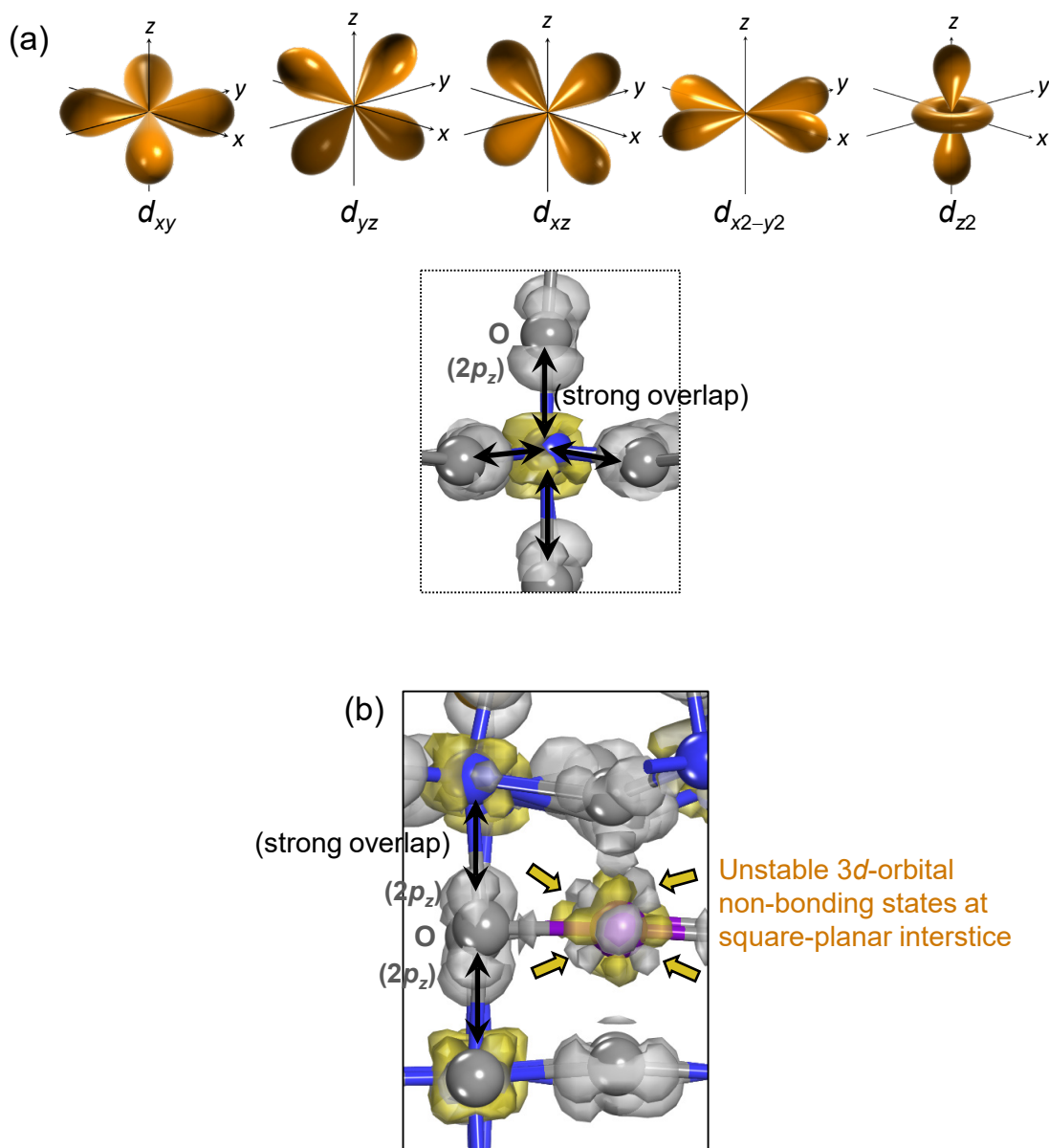
Figure S9. Instability of transition-metal cations in the square-planar interstices at a GB. (**a**) The shapes of five 3d orbitals (d_{xy}, d_{yz}, d_{xz}, d_{x2-y2}, and d_{z2}) are schematically described. As oxygen ligands place on each of the x, y, and z axes to construct six-coordination octahedra, the five 3d orbitals from a transition metal can be easily hybridized with the 2p_z orbitals of six neighboring oxygen ligands, as denoted by black arrows in the illustration. (**b**) However, if the added transition metals occupy the interstices, there are no available O 2p_z orbitals for hybridization with the 3d orbitals of the interstitial metals. Note that all the oxygen octahedra in perovskite oxides are connected with each other in a corner-sharing manner. Consequently, the 2p_z orbitals from each oxygen ligand are already hybridized with the 3d orbitals of two neighboring Ti cations, as denoted by black arrows. Unless the neighboring oxygen atoms strongly displace toward the dopants at the interstices for the orbital hybrid, the instability of the non-bonding 3d states is difficult to avoid.
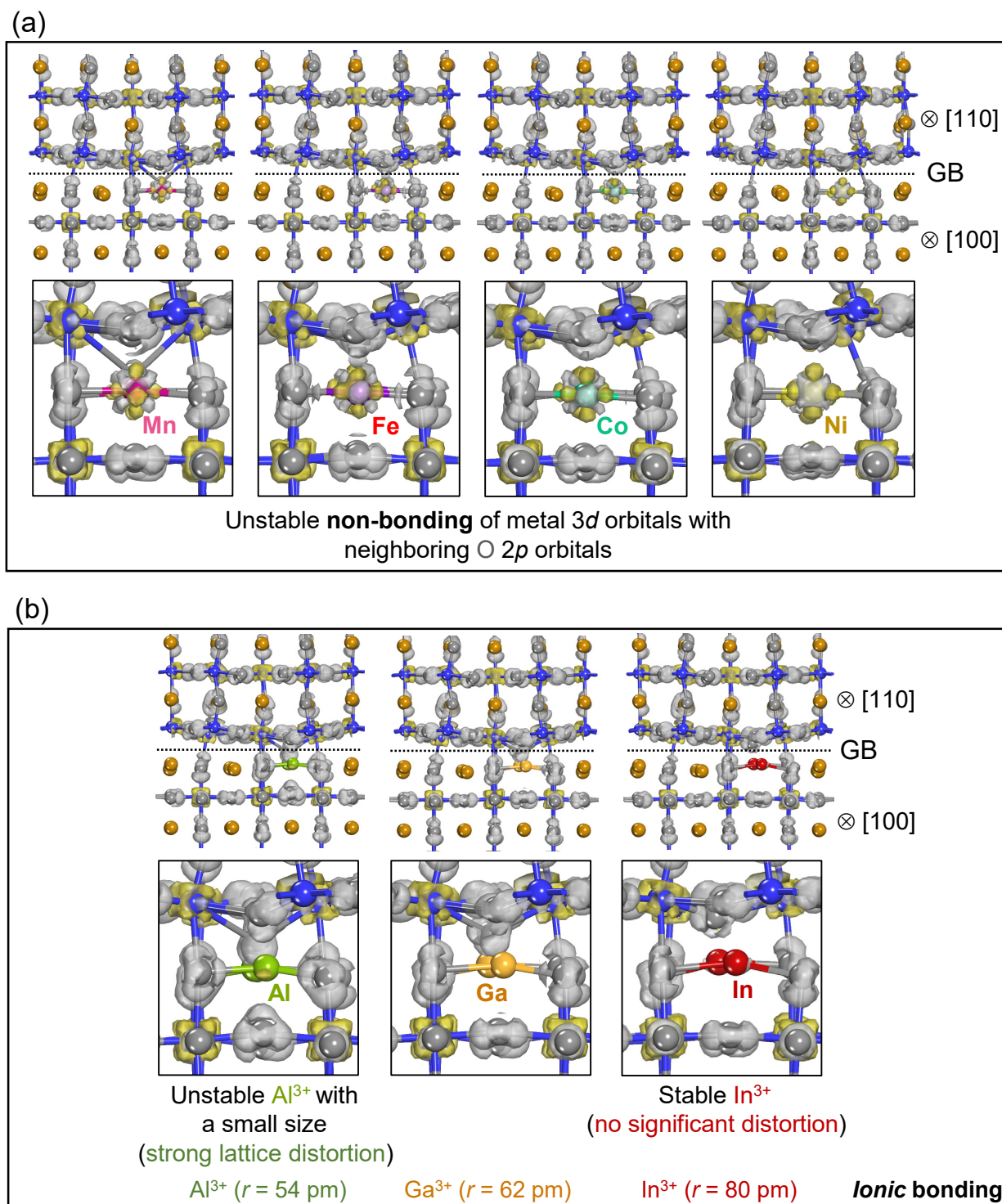
Figure S10. Entire set of electron-density isosurface contours for the seven dopants in the interstitial position at a GB. (**a**) For the four transition-metal dopants, Mn, Fe, Co and Ni, at the interstice, the non-bonding 3d orbitals are visualized in each of the contour maps. (**b**) For the other three dopants, Al, Ga, and In, which show ionic bonding characteristics, the stability at the square-planar interstice is determined by their ionic size relative to that of the oxygen anion on the basis of Pauling's first rule.
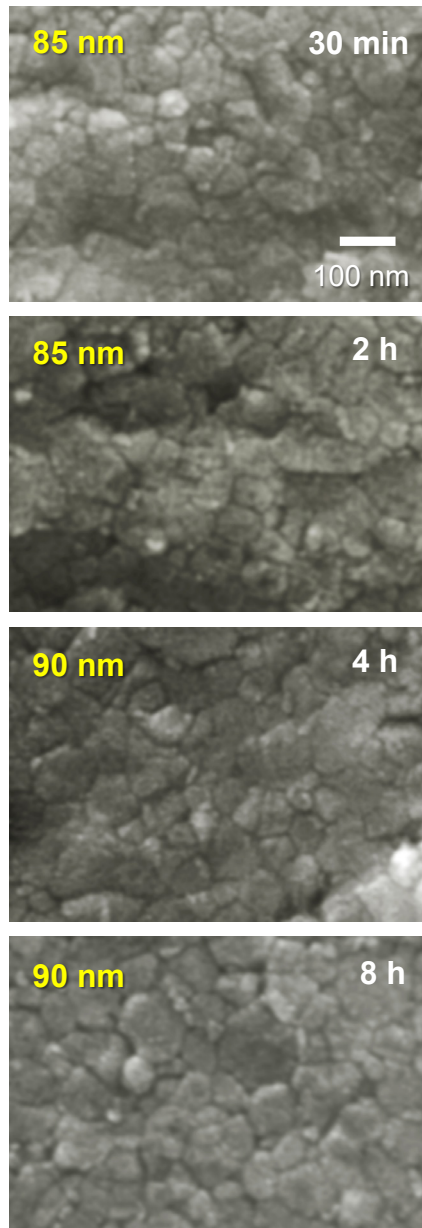
Figure S11. Scanning electron microscopy (SEM) images showing the microstructure of In-added samples. The samples were fabricated from 60-nm BaTiO$_3$ nanoparticles and sintered at 1220°C in 0.5H$_2$–99.5N$_2$ for 30 min, 2 h, 4 h, and 8 h. It is noted that the grain size hardly varies with sintering time, directly showing that grain-boundary migration is strongly inhibited by In segregation at GBs.
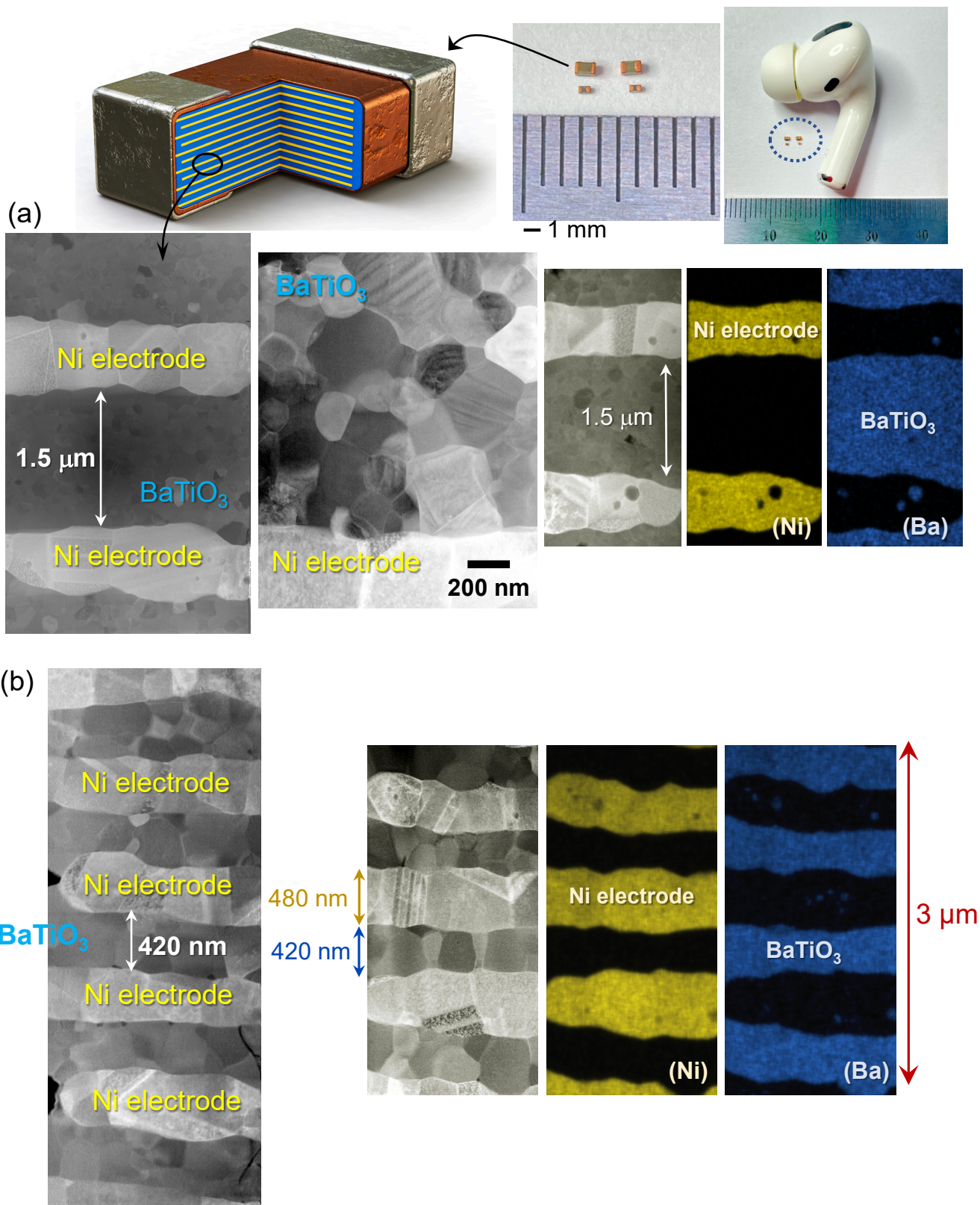
Figure S12. Internal structure of commercially available BaTiO$_3$-based MLCCs. (**a**) A micron-scale thickness of BaTiO$_3$ layers in a typical X7R-grade MLCC is demonstrated. (**b**) A cross-sectional STEM image is provided to show the configuration of a state-of-the-art MLCC, having 362 layers, used in current smartphones. A large number of BaTiO$_3$ layers with <500 nm thickness are stacked together with Ni electrode layers.
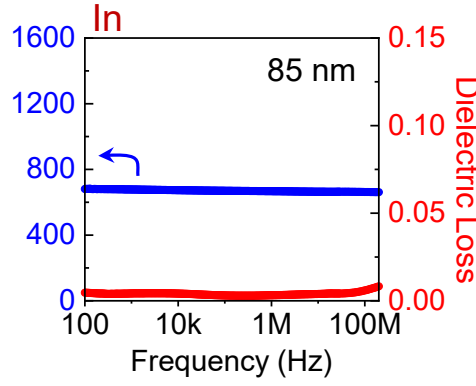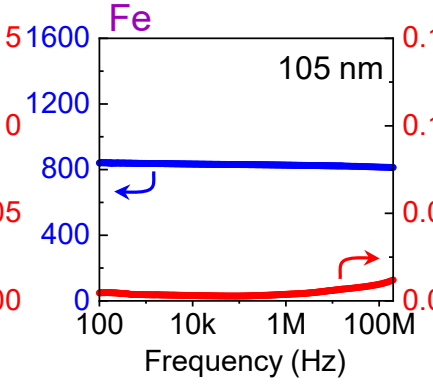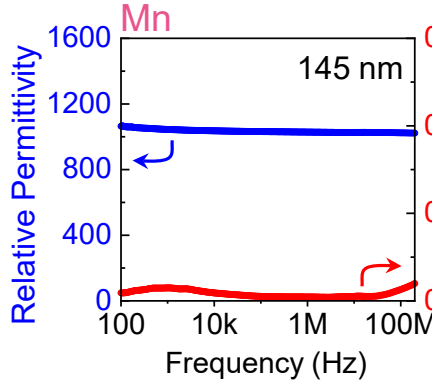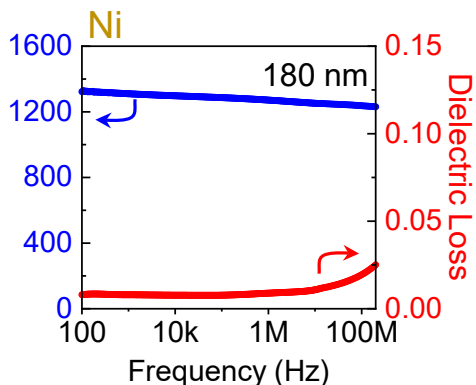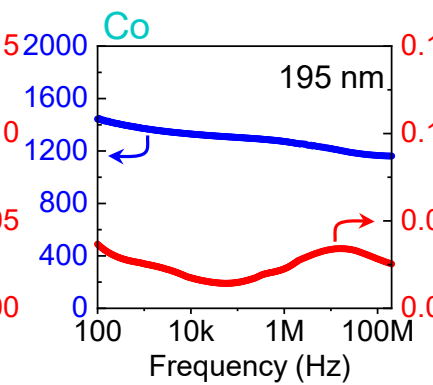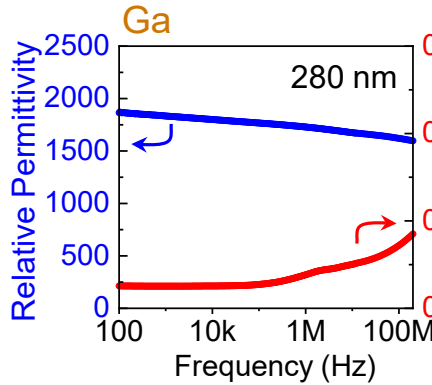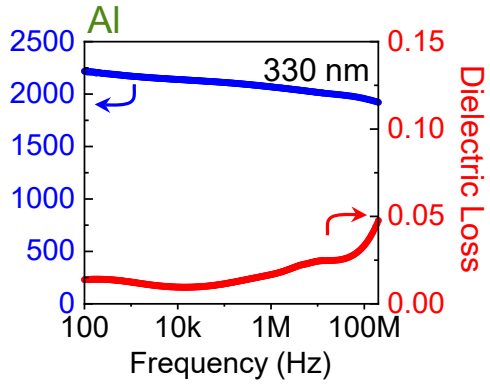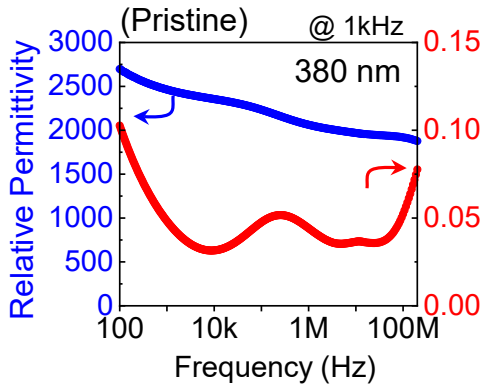
Figure S13. Dielectric properties of polycrystalline samples with the seven additives. Grain-size-dependent relative permittivity is consistently observed. A significant reduction of dielectric loss is also identified in general, when the grain size becomes smaller.
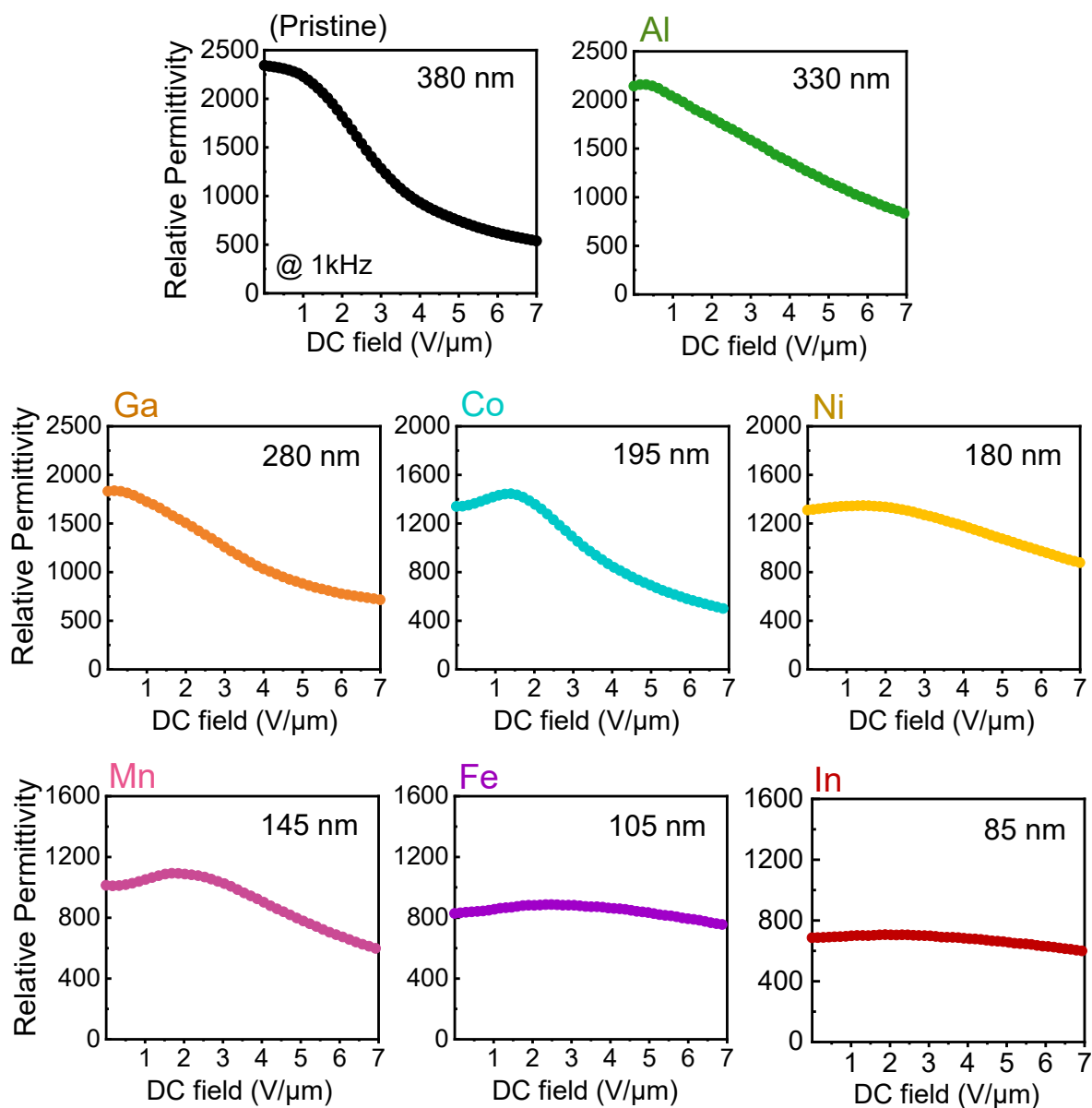
Figure S14. DC-bias-dependent relative permittivity variations. This set of measurement results emphasizes that the nominally high permittivity of >2000 can seriously diminish when a large DC field is applied. For example, the permittivity value of 2340 at 0 V in the 380-nm pristine sample reduces to less than 600 under 7 V/μm, marking more than a 70% reduction in permittivity. Therefore, it is apparent that the control of grain size and subsequent ferroelectricity is of significance to acquire higher *effective* permittivity with better stability under DC bias.

Upper temperature limit	Capacitance variation
4= +65°C	P= ±10%
5= +85°C	R= ±15%
6= +105°C	S= ±22%
7= +125°C	T= +22/-33%
8= +150°C	U= +22/-56%
9= +200°C	V= +22/-82%
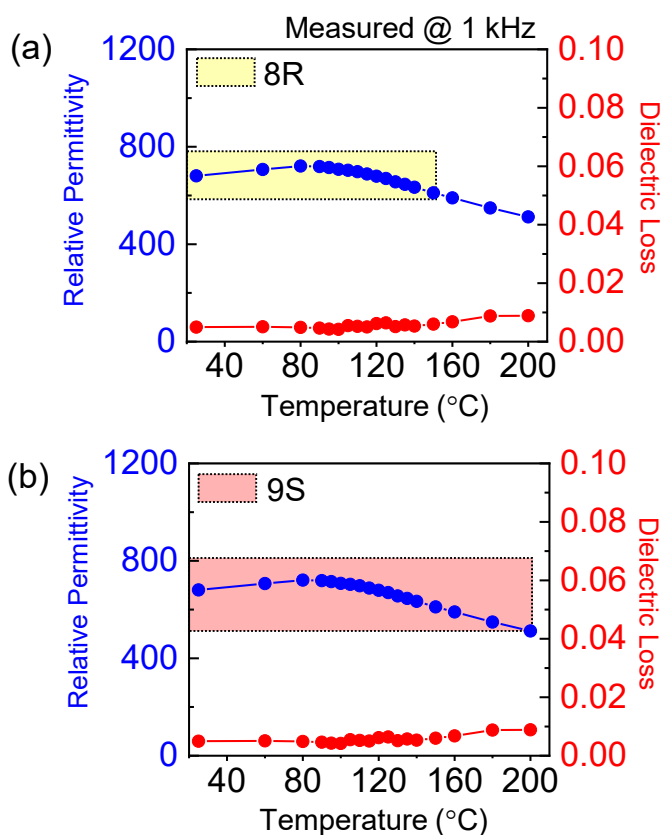
Figure S15. Classification of code system for temperature stability. Information on the number codes for the upper temperature limit and the letter code for allowed capacitance variation is provided in the table. (**a**) The range of permittivity and temperature variations for grade 8R is denoted by yellow shading in the plot of the In-added 85-nm sample. This indicates that the condition of grade 8R is satisfied in this sample. (**b**) Red shading in this same plot denotes the tolerance range for grade 9S capacitors. This sample satisfies the requirements for grade 9S overall, except the slight deviation over 180°C.

Figure S16. Observation of ferroelectric domains in polycrystalline BaTiO$_3$. As the average grain size becomes small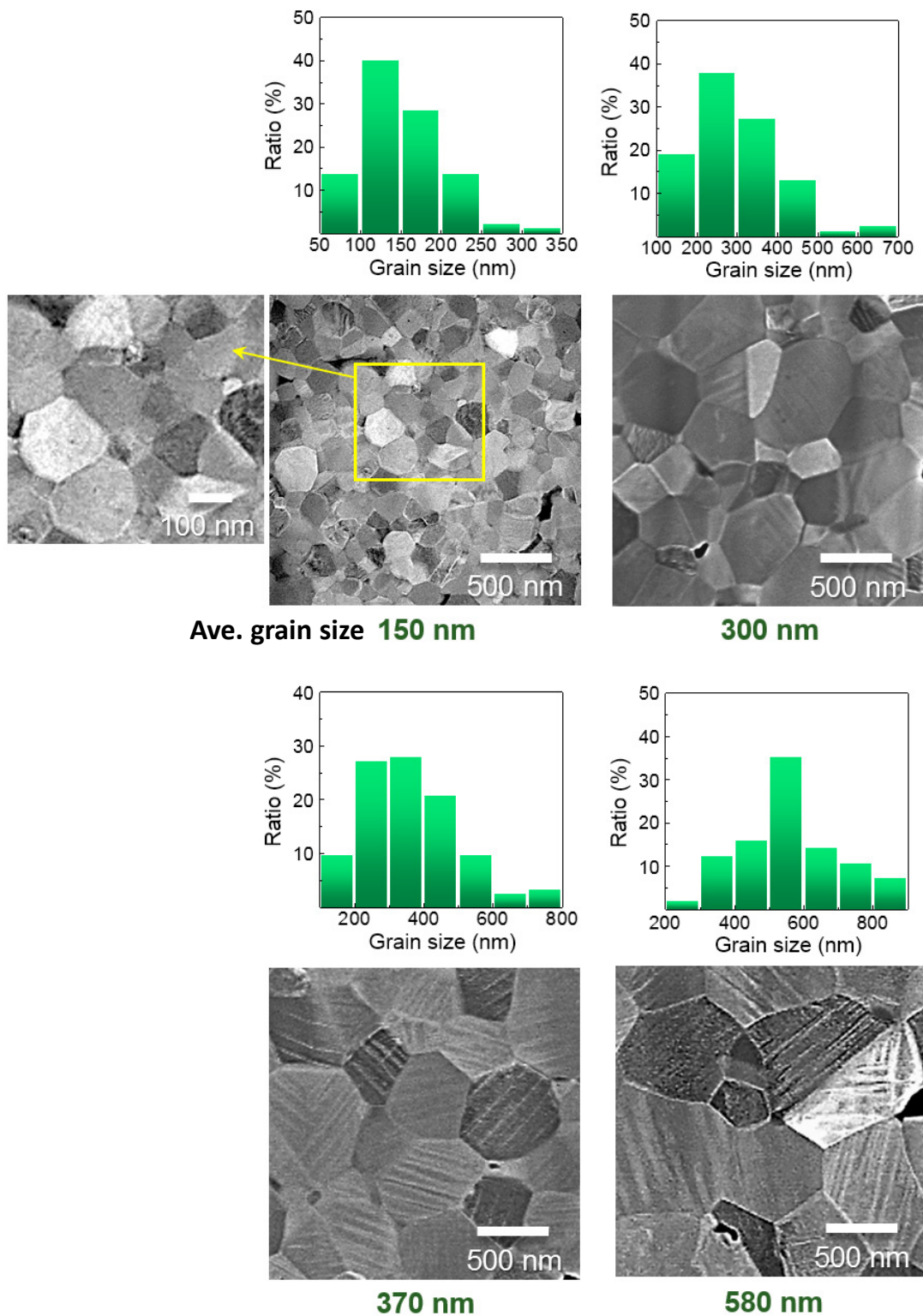, clear observation of the domains becomes difficult. This is consistent with the grain-size-dependent ferroelectricity with reduced tetragonality.
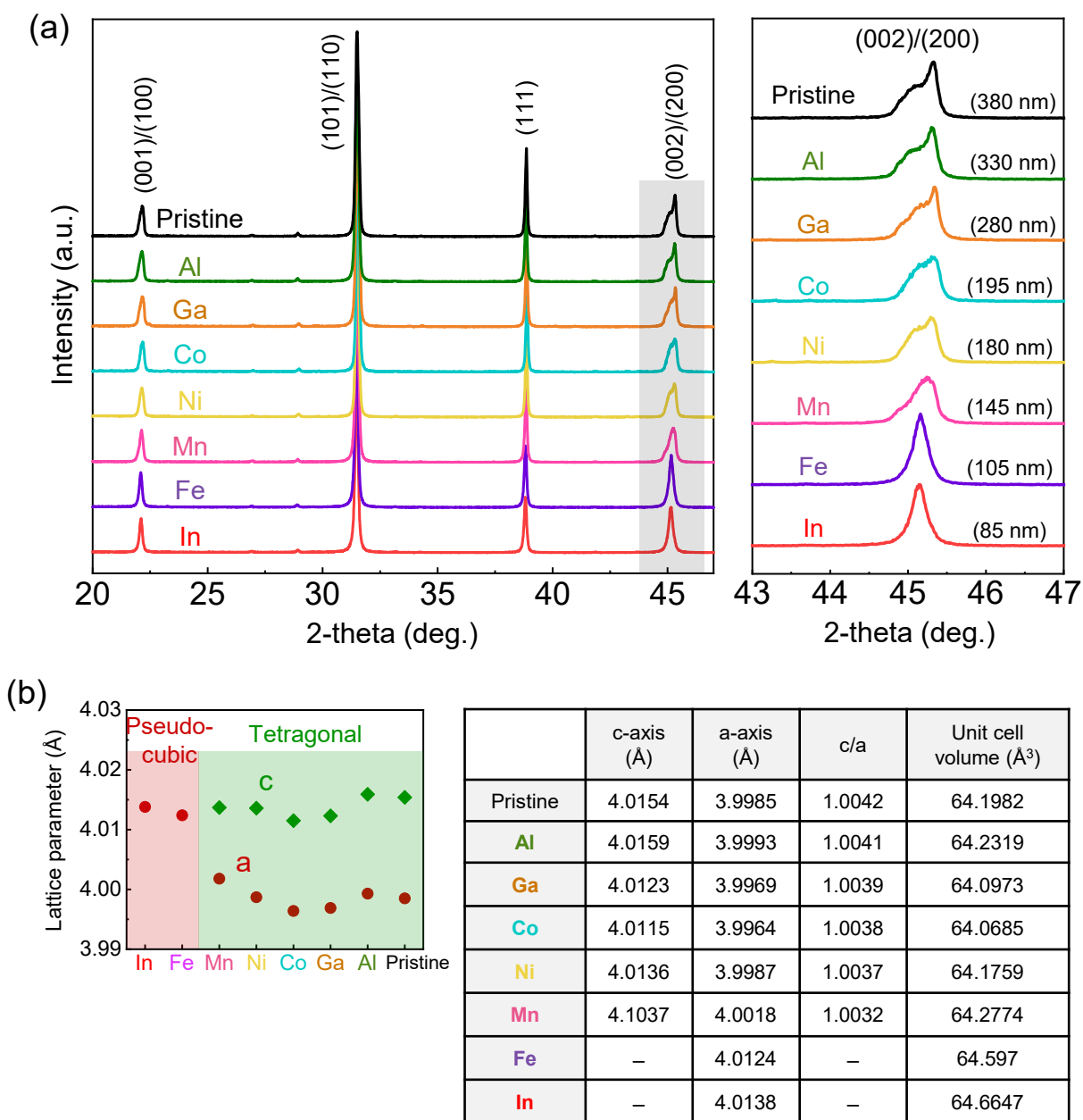
(a) Left panel: X-ray diffraction patterns labeled Pristine, Al, Ga, Co, Ni, Mn, Fe, In with peaks (001)/(100), (101)/(110), (111), (002)/(200). X-axis: 2-theta (deg.) from 20 to 45. Y-axis: Intensity (a.u.).

Right panel: (002)/(200) peaks with grain sizes — Pristine (380 nm), Al (330 nm), Ga (280 nm), Co (195 nm), Ni (180 nm), Mn (145 nm), Fe (105 nm), In (85 nm). X-axis: 2-theta (deg.) from 43 to 47.

(b) Lattice parameter (Å) plot: Pseudo-cubic region (In, Fe), Tetragonal region (Mn, Ni, Co, Ga, Al, Pristine), showing c and a parameters.

	c-axis (Å)	a-axis (Å)	c/a	Unit cell volume (Å³)
Pristine	4.0154	3.9985	1.0042	64.1982
Al	4.0159	3.9993	1.0041	64.2319
Ga	4.0123	3.9969	1.0039	64.0973
Co	4.0115	3.9964	1.0038	64.0685
Ni	4.0136	3.9987	1.0037	64.1759
Mn	4.1037	4.0018	1.0032	64.2774
Fe	–	4.0124	–	64.597
In	–	4.0138	–	64.6647

Figure S17. Additional sets of X-ray diffraction patterns. (**a**) No significant position variation of the Bragg peaks is noted. In addition, the tetragonality of $BaTiO_3$ begins to substantially diminish and transforms into a pseudo-cubic structure when the particle size becomes small (right-hand panel). No obvious peak splitting of the (002) and (200) reflections at $2\theta \sim 45°$ is observable in the Fe- and In-added samples, the grain sizes of which are 105 and 85 nm, respectively. (**b**) The information on the lattice parameters and unit-cell volumes acquired from the diffraction patterns is provided for each sample.